ELECTRONIC SUPPLEMENTARY INFORMATION (ESI)

Construction of an $Au_{12}Cd_2$ nanocluster with circularly polarized luminescence by a metal- and ligand-exchange strategy

Jun Zhou,[‡a] Xiaofei Yang,[‡a] Peisen Zheng,[‡a] Qinzhen Li,[a] Xiaowu Li,[a] Jinsong Chai,[a] Baoyu Huang,[*b] Sha Yang[*a] and Manzhou Zhu[*a]

[a] Department of Chemistry and Centre for Atomic Engineering of Advanced Materials, Key Laboratory of Structure and Functional Regulation of Hybrid Materials of Ministry of Education, Institutes of Physical Science and Information Technology, and Anhui Province Key Laboratory of Chemistry for Inorganic/Organic Hybrid Functionalized Materials, Anhui University, Hefei, Anhui 230601, China.
[b] Hunan Provincial Key Laboratory of Environmental Catalysis & Waste Recycling, College of Materials and Chemical Engineering, Hunan Institute of Engineering, Xiangtan 411104, China.

*E-mails of corresponding authors: yangshac@ahu.edu.cn (S.Y.); 22164@hnie.edu.cn (B.H.); zmz@ahu.edu.cn (M.Z.).

Notes: The authors declare no competing financial interest.

‡ Jun Zhou, Xiaofei Yang and Peisen Zheng contributed equally to this work.

This Supporting Information includes: Scheme S1, Fig. S1-S38 and Tables S1-S8†.

Experimental

Preparation of R/S-fenchylthiol ligand

Currently, the price of commercially available organic thiol ligands with a single chiral configuration is relatively expensive, which limits their application and development. By contrast, the acquisition of natural products is very convenient. The 1-adamantanethiol ligand of $Au_{14}Cd_1(SAdm)_{12}$ nanocluster selected in this work belong to large steric thiol ligands, so we selected fenchone (a nature product), a similar large hindered steric ligand, as the raw material to synthesize a fenchylthiol ligand.

(+)-fenchone (or (−)-fenchone) and Lawson reagent were dissolved in anhydrous toluene with a molar ratio of 1:0.6. After stirring at 90 °C for 2 hours, the color of the solution turned to red. Through the first chromatographic separation, a red substance can be obtained. Then, 75 mL of 1,2-dimethoxyethane and 800 mg of sodium borohydride were added to the collected red solution, which was further slowly stirred to fully react. After the reaction is complete, the crude product is separated by chromatography to obtain high-purity R/S-fenchylthiol (≥98%) (Fig. S1†).

Characterization of R/S-fenchylthiol ligands

R/S-fenchylthiol ligands were characterized by gas-chromatography-mass spectrometry (GC-MS) and nuclear magnetic resonance spectroscopy (NMR). The test results of R/S-fenchylthiol ligands are shown in Fig. S2-S7†. As shown in Fig. S2†, four resonances (2.63 ppm, 1.74 ppm, 1.64-1.26 ppm, and 1.05-0.91 ppm) were found in the ^{1}H-NMR spectrum for S-fenchylthiol dissolved in CD_3Cl. Therefore, the structure of S-fenchylthiol was determined from the ^{1}H NMR spectrum. There are ten peaks can be found in ^{13}C-NMR, with ten single peaks at 58.41, 50.04, 48.08, 43.60, 39.58, 31.24, 26.76, 26.19, 23.48, and 20.31, corresponding to the ten carbon atoms in the thiol (Fig. S3†). Moreover, with the help of GC-MS, the purity as well as the molecular formula of the synthesized S-fenchylthiol ligand were confirmed. The intense peak at 170.08 Da in the GC-MS spectrum can be assigned to the formula of *S*-$C_{10}H_{17}SH$ (calculated: 170.11 Da, Fig. S6†). For R-fenchylthiol, the molecular formula and structure were also characterized by ^{1}H NMR, ^{13}C NMR and GC-MS (Fig. S4, S5, S7†).

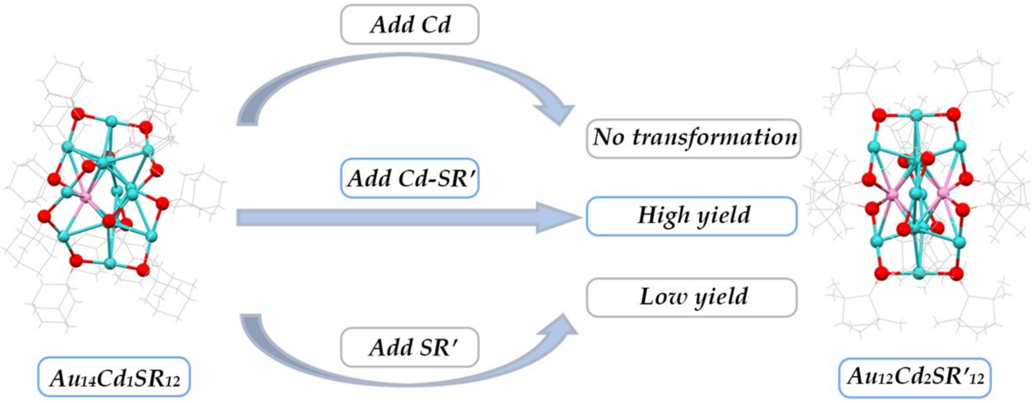

Scheme S1 Transformation pathways from $Au_{14}Cd_1$ to *R/L*-$Au_{12}Cd_2$ nanoclusters

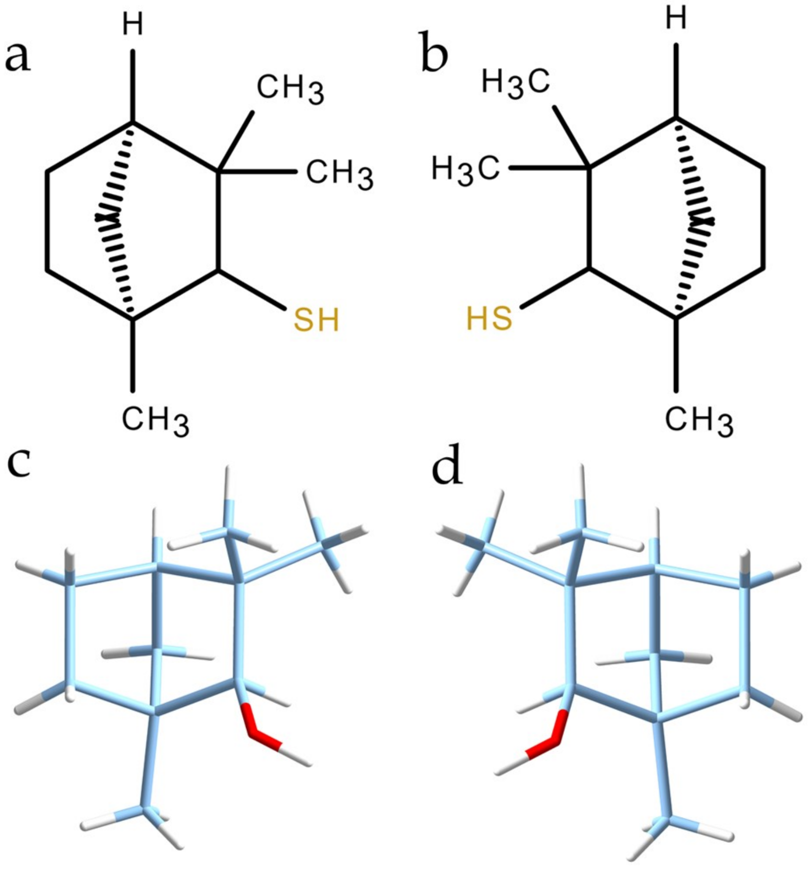

Fig. S1 Chemical structures of *R*-fenchylthiol (*R*-$C_{10}H_{17}SH$, (1R,4S)-1,3,3-trimethylbicyclo[2.2.1]heptan-2-thiol) (a) and *S*-fenchylthiol (*S*-$C_{10}H_{17}SH$, (1S,4R)-1,3,3-trimethylbicyclo[2.2.1]heptan-2-thiol) (b); Molecular structures of *R*-fenchylthiol (*R*-$C_{10}H_{17}SH$) (c); and *S*-fenchylthiol (*S*-$C_{10}H_{17}SH$) (d). (Color labels: Sky blue = C, red = S, white = H.)

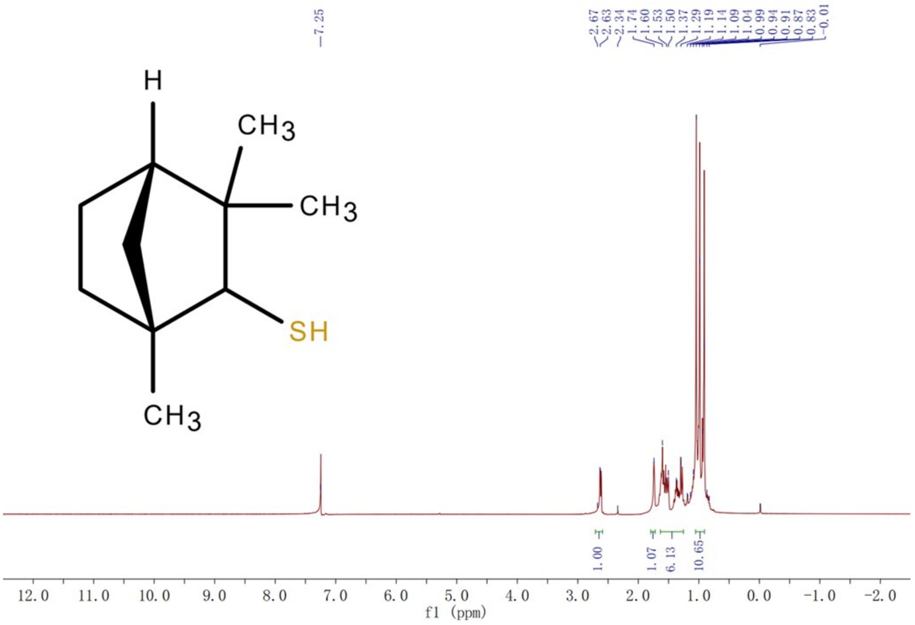

Fig. S2 ^{1}H NMR spectrum of *S*-$C_{10}H_{17}SH$ (in $CDCl_3$).

^{1}H NMR (400 MHz, Chloroform-*d*) δ 2.63 (s, 1H), 1.74 (s, 1H), 1.63 - 1.25 (m, 6H), 1.05 - 0.91 (m, 10H).

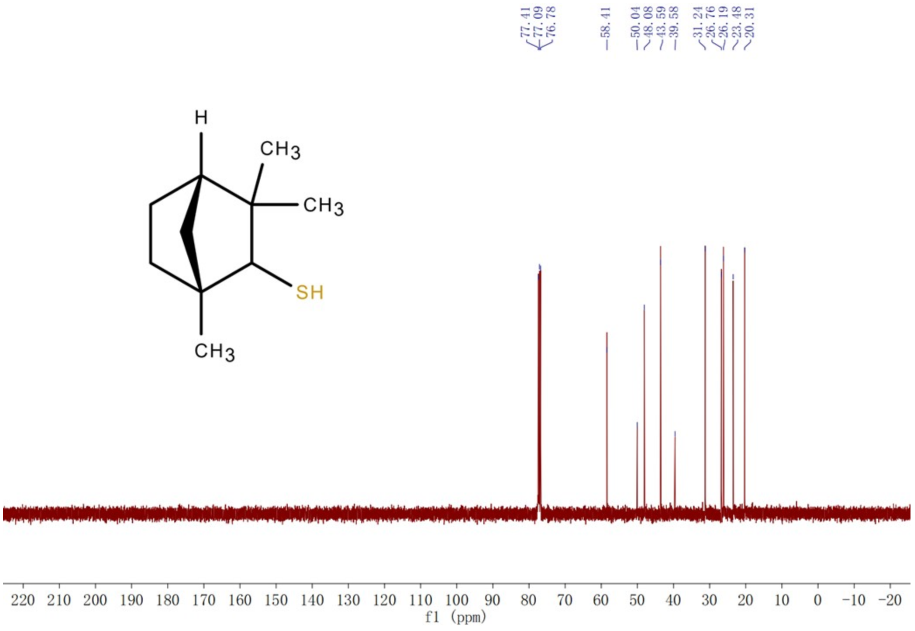

Fig. S3 ^{13}C NMR spectrum of *S*-$C_{10}H_{17}SH$ (in $CDCl_3$).

^{13}C NMR (101 MHz, Chloroform-*d*) δ 58.41, 50.04, 48.08, 43.59, 39.58, 31.24, 26.76, 26.19, 23.48, 20.31.

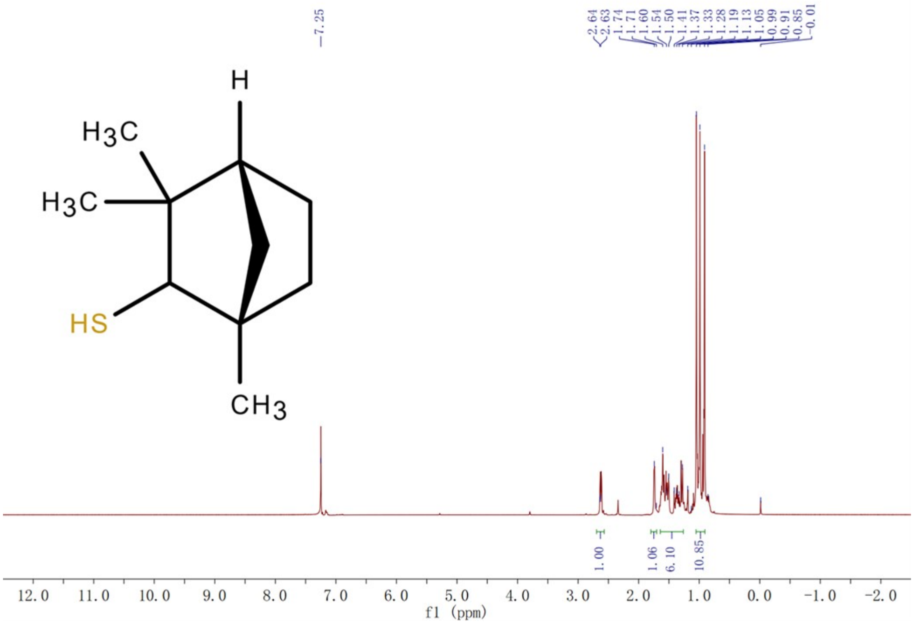

Fig. S4 ^{1}H NMR spectrum of *R*-$C_{10}H_{17}SH$ (in $CDCl_3$).

^{1}H NMR (400 MHz, Chloroform-*d*) δ 2.63 (d, *J* = 6.8 Hz, 1H), 1.74 (s, 1H), 1.64 - 1.26 (m, 6H), 1.05 - 0.91 (m, 10H).

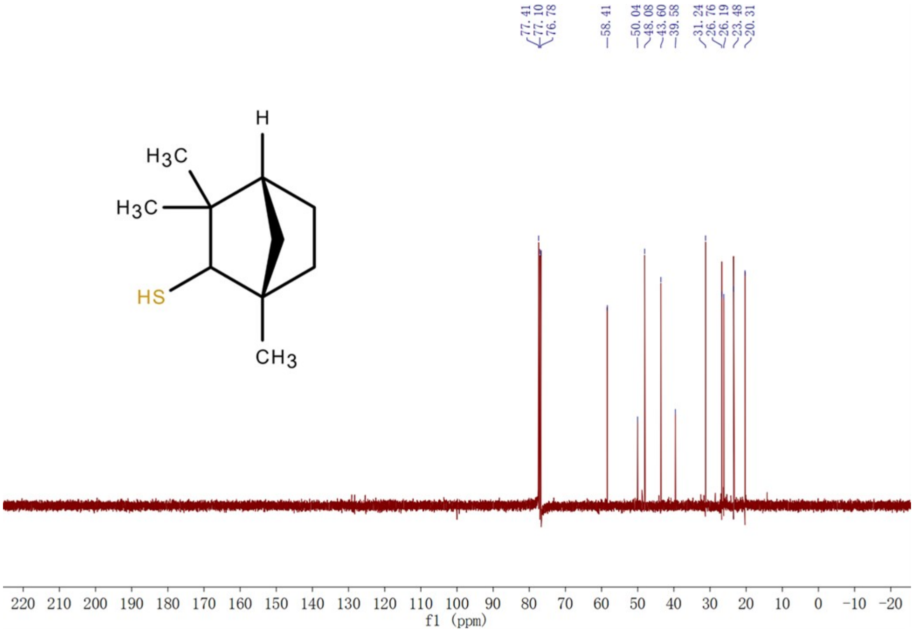

Fig. S5 ^{13}C NMR spectrum of *R*-$C_{10}H_{17}SH$ (in $CDCl_3$).

^{13}C NMR (101 MHz, Chloroform-*d*) δ 58.41, 50.04, 48.08, 43.60, 39.58, 31.24, 26.76, 26.19, 23.48, 20.31.

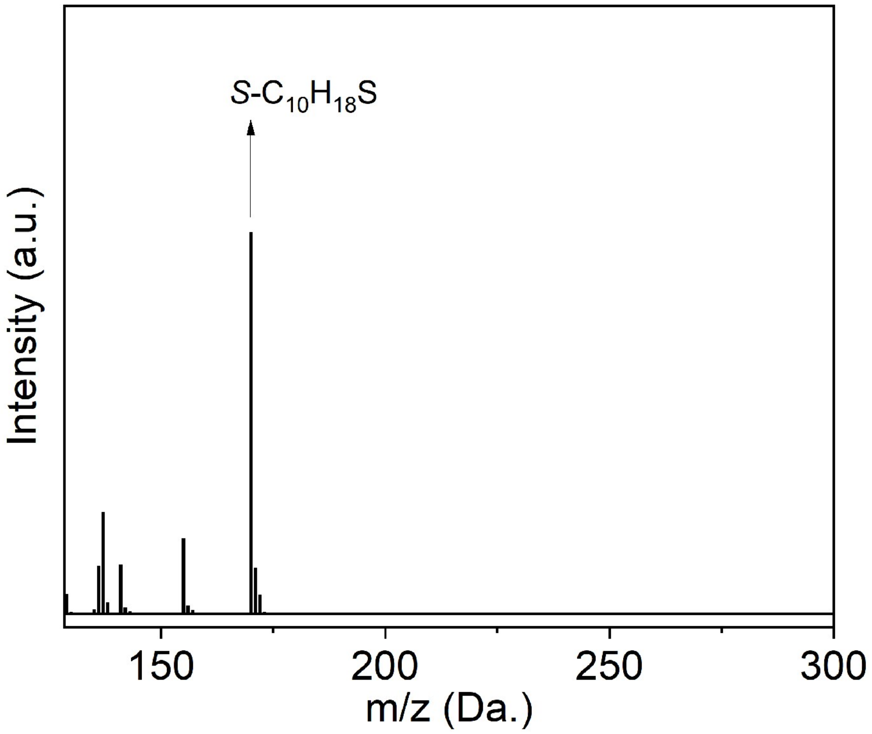

Fig. S6 GC-MS spectrum of *S*-$C_{10}H_{17}SH$.

The intense peak at 170.08 Da in the GC-MS spectrum can be assigned to the formula of *S*-$C_{10}H_{17}SH$ (calculated: 170.11 Da).

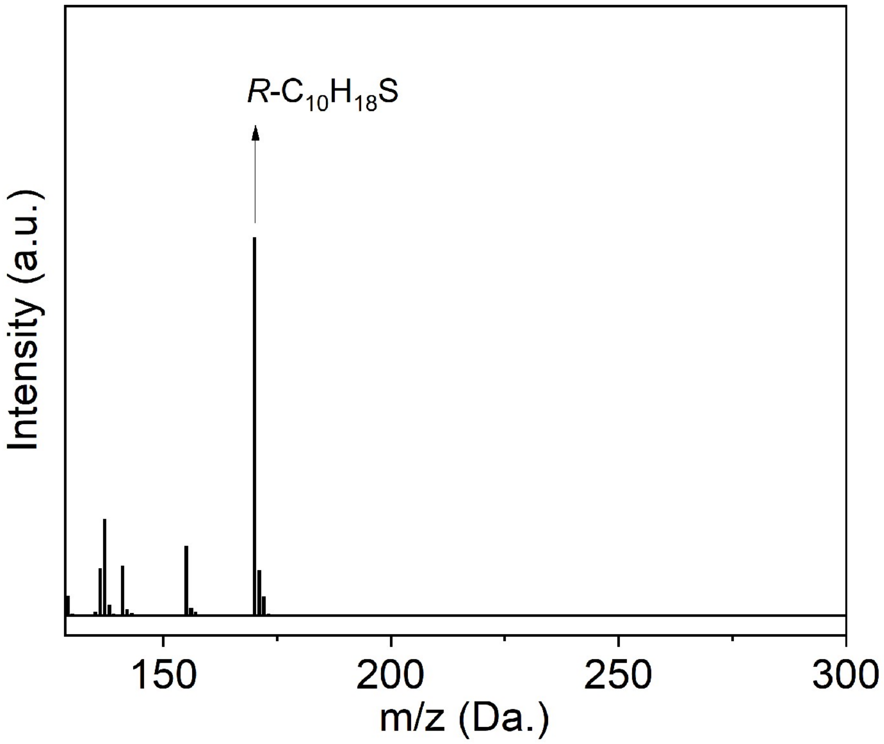

Fig. S7 GC-MS spectrum of *R*-$C_{10}H_{17}SH$.

The intense peak at 170.08 Da in the GC-MS spectrum can be assigned to the formula of *R*-$C_{10}H_{17}SH$ (calculated: 170.11 Da).

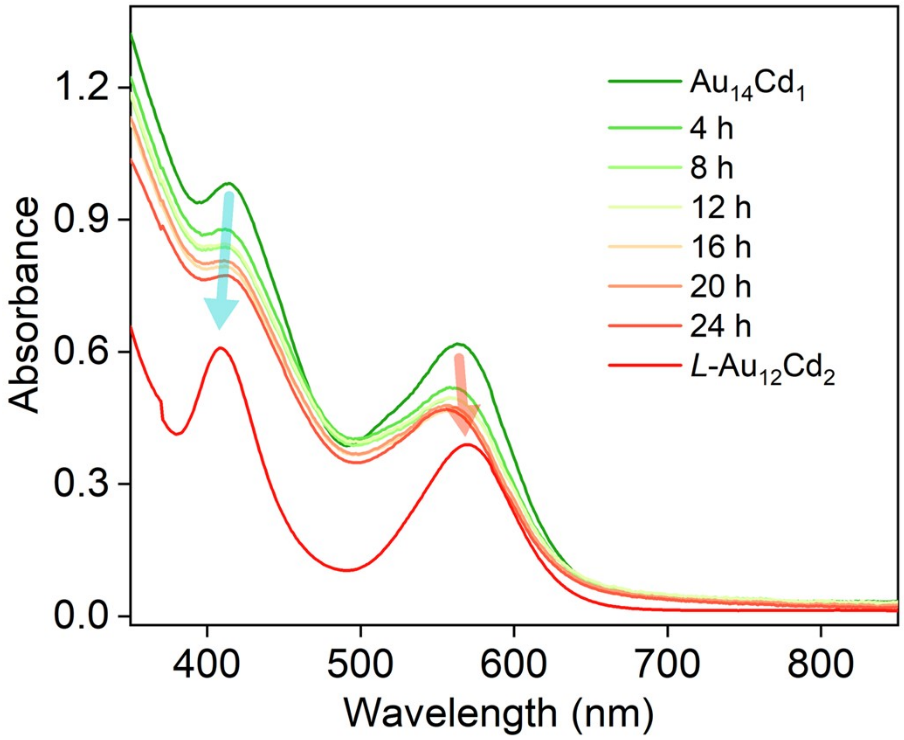

Fig. S8 Time dependent UV-vis absorbance spectra of tracking process from $Au_{14}Cd_1$ to *L*-$Au_{12}Cd_2$ (Add Cd-SR-(+) complex).

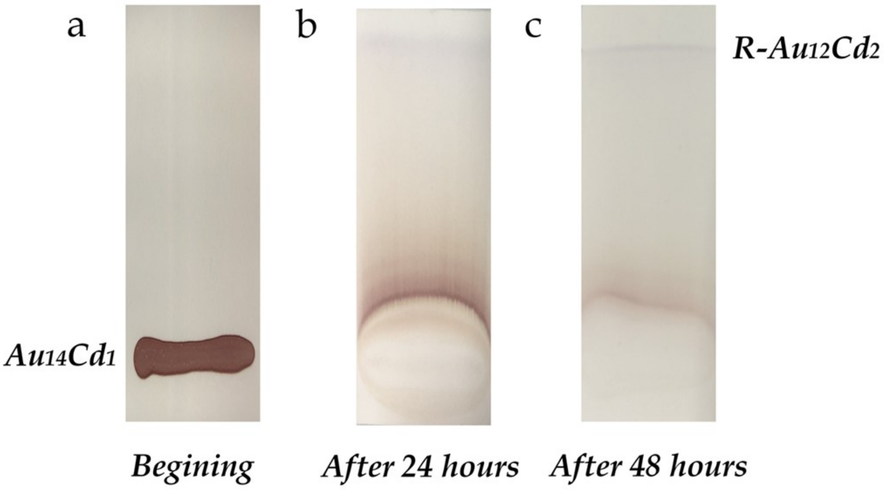

Fig. S9 Time dependent thin-layer chromatography plates pictures of tracking process from $Au_{14}Cd_1$ to *R*-$Au_{12}Cd_2$ (Add *R*-Fenchethiol ligand).

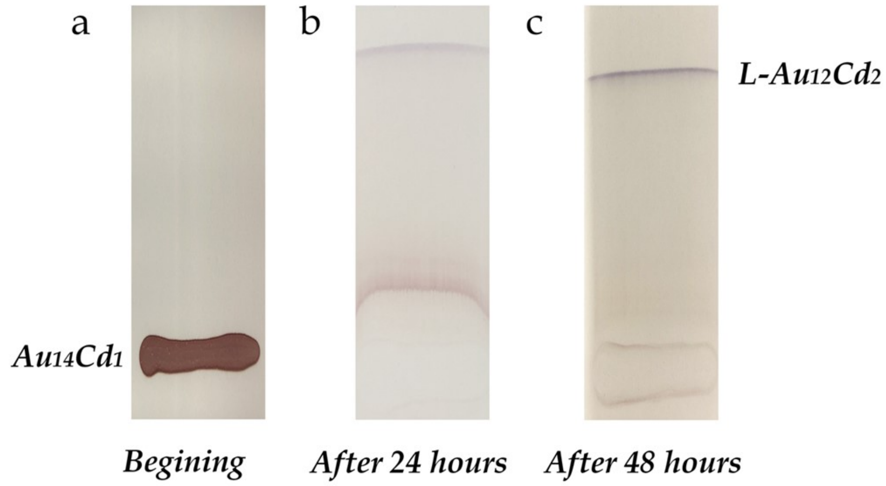

Fig. S10 Time dependent thin-layer chromatography plates pictures of tracking process from $Au_{14}Cd_1$ to *L*-$Au_{12}Cd_2$ (Add *S*-Fenchethiol ligand).

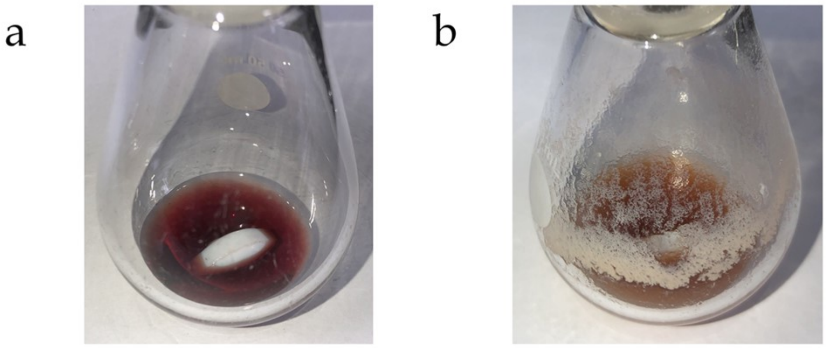

Fig. S11 $Au_{14}Cd_1$ reacted with the cadmium chloride (a) before and (b) after.

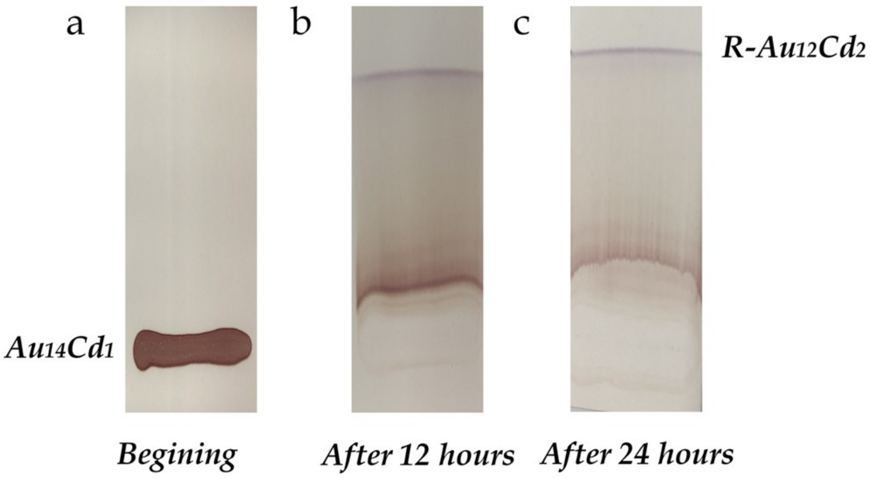

Fig. S12 Time dependent thin-layer chromatography plates pictures of tracking process from $Au_{14}Cd_1$ to *R*-$Au_{12}Cd_2$ (Add Cd-SR-(-) complex).

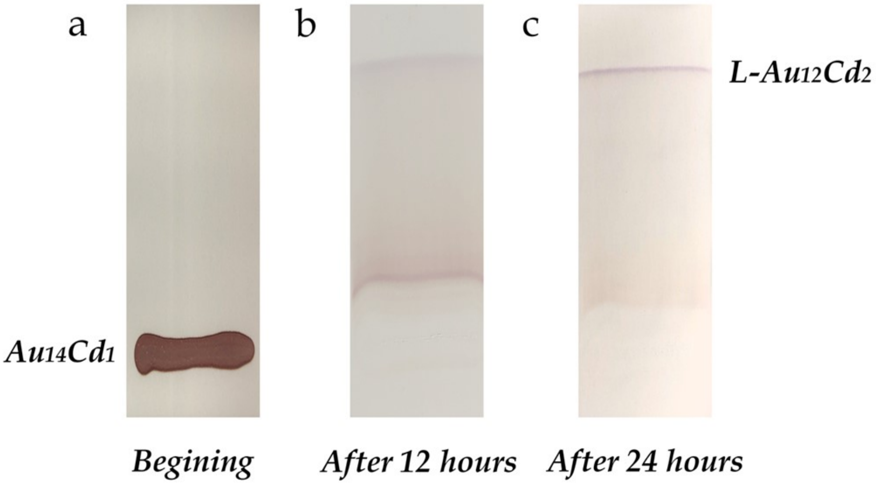

Fig. S13 Time dependent thin-layer chromatography plates pictures of tracking process from $Au_{14}Cd_1$ to *L*-$Au_{12}Cd_2$ (Add Cd-SR-(+) complex).

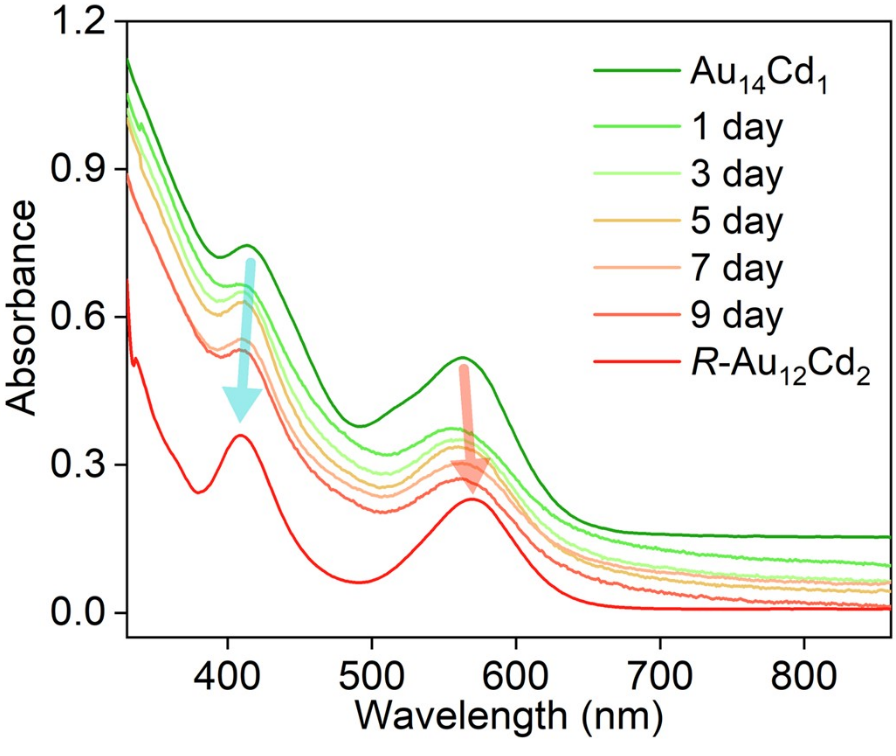

Fig. S14 Time dependent UV-vis absorbance spectra of tracking process from $Au_{14}Cd_1$ to *R*-$Au_{12}Cd_2$ (Add (-)-Fenchethiol ligand).

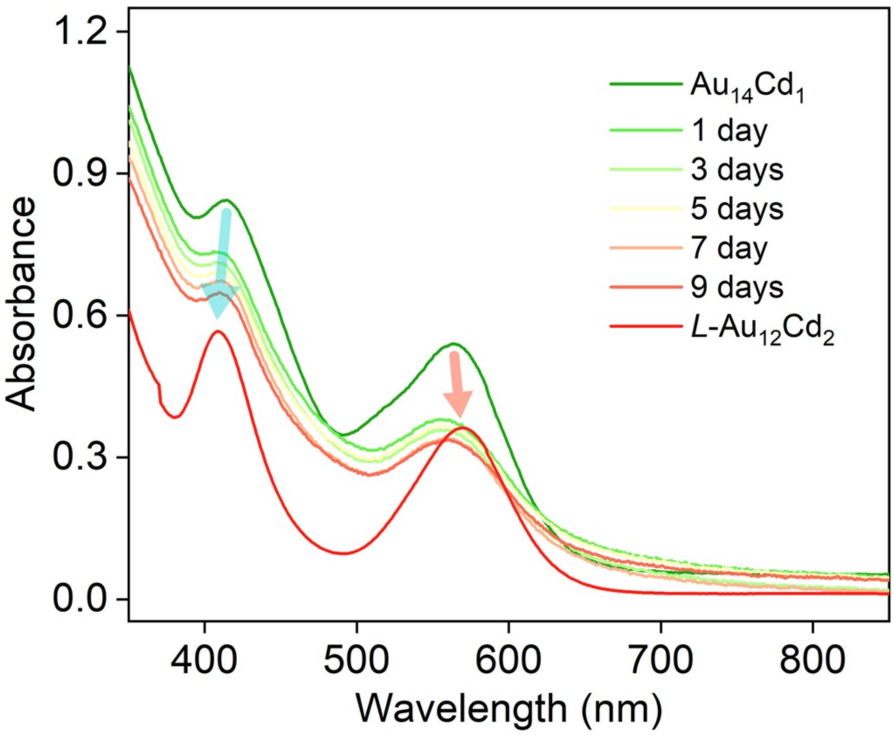

Fig. S15 Time dependent UV-vis absorbance spectra of tracking process from $Au_{14}Cd_1$ to L-$Au_{12}Cd_2$ (Add (+)-Fenchethiol ligand).

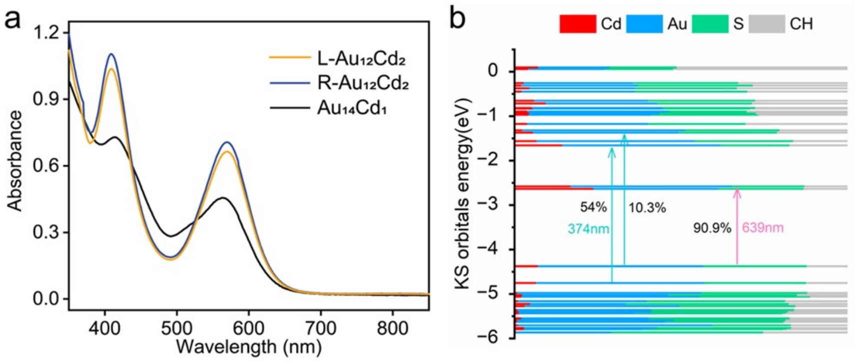

Fig. S16 (a) Comparison of the UV-vis spectra of L/R-$Au_{12}Cd_2$ and $Au_{14}Cd_1$; (b) Kohn-Sham molecular orbital energy level diagram of L/R-$Au_{12}Cd_2$ for absorption.

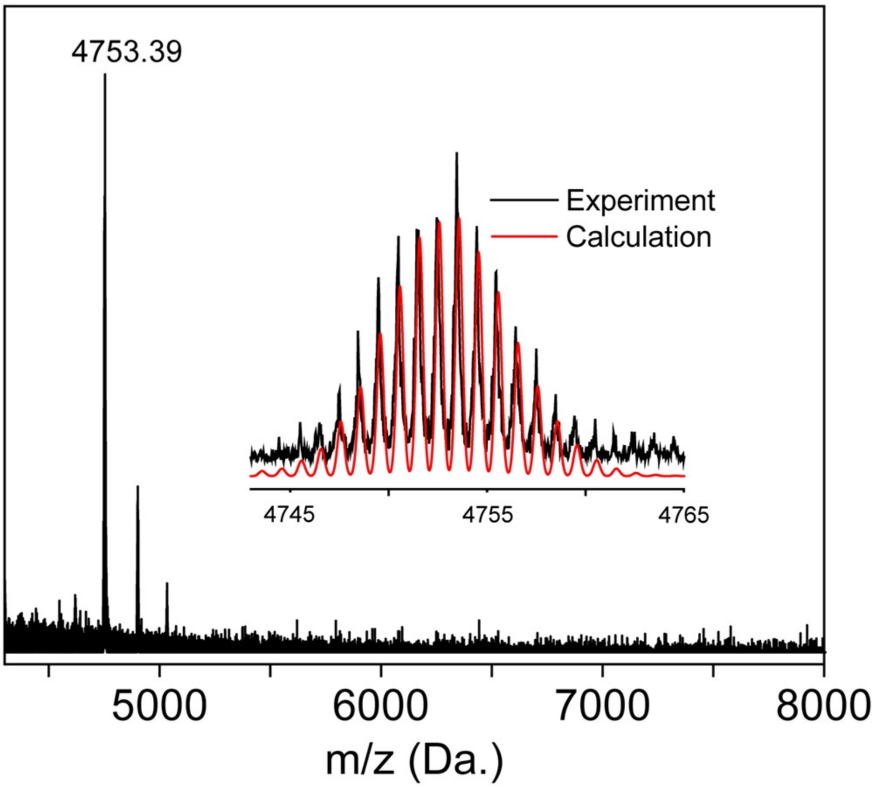

Fig. S17 ESI-MS of *L*-$Au_{12}Cd_2$ nanocluster in CH_2Cl_2. Inset shows the experimental and calculated isotopic patterns of [*L*-$Au_{12}Cd_2(C_{10}H_{17}S)_{12}Cs]^+$.

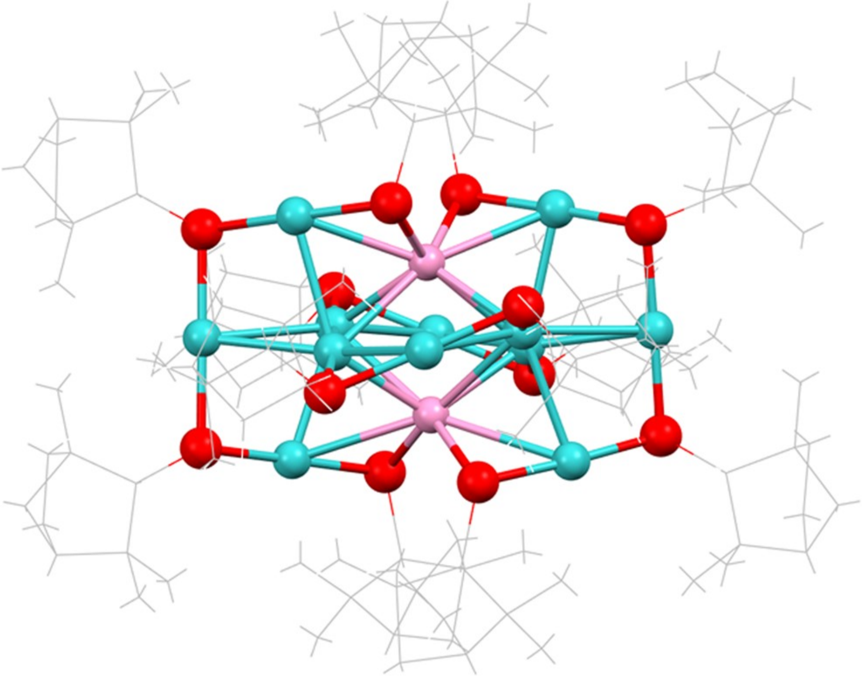

Fig. S18 Full structure of *L*-$Au_{12}Cd_2$ (Color labels: blue = Au, pink = Cd, red = S, and gray sticks = C. All the hydrogen atoms have been omitted for clarity).

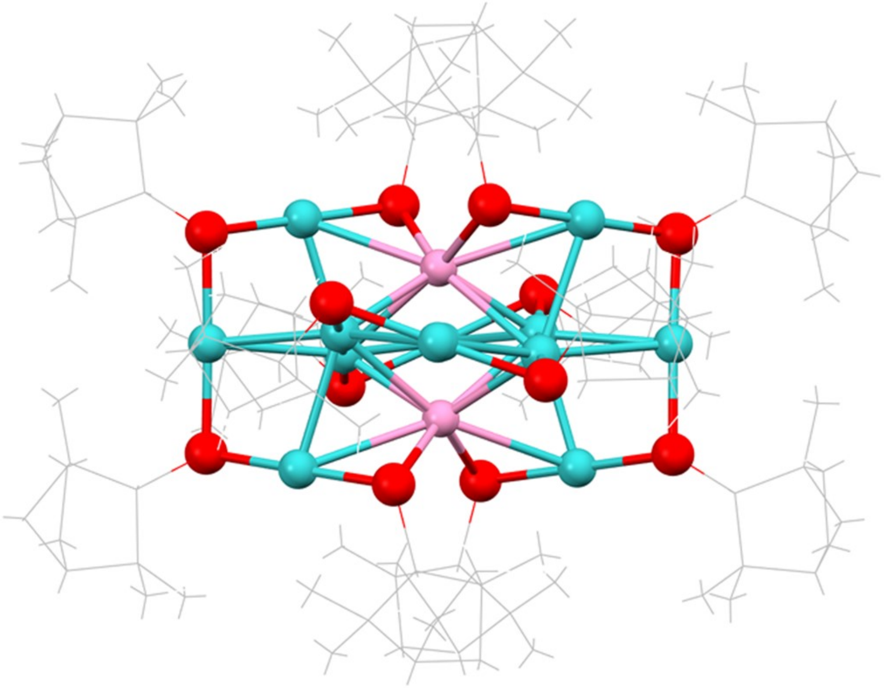

Fig. S19 Full structure of *R*-$Au_{12}Cd_2$ (Color labels: blue = Au, pink = Cd, red = S, and gray sticks = C. All the hydrogen atoms have been omitted for clarity).

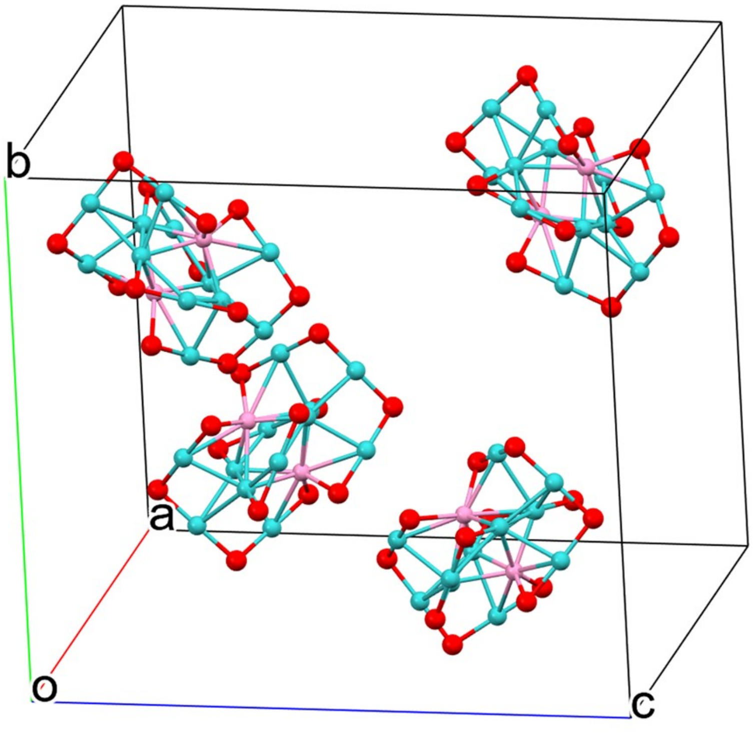

Fig. S20 A unit cell of *L*-$Au_{12}Cd_2$ and label O means the original point of unit cell and labels of a, b, as well as c are the crystal orientation (Color labels: blue = Au, pink = Cd, red = S. All carbon atoms and hydrogen atoms are omitted for clarity).

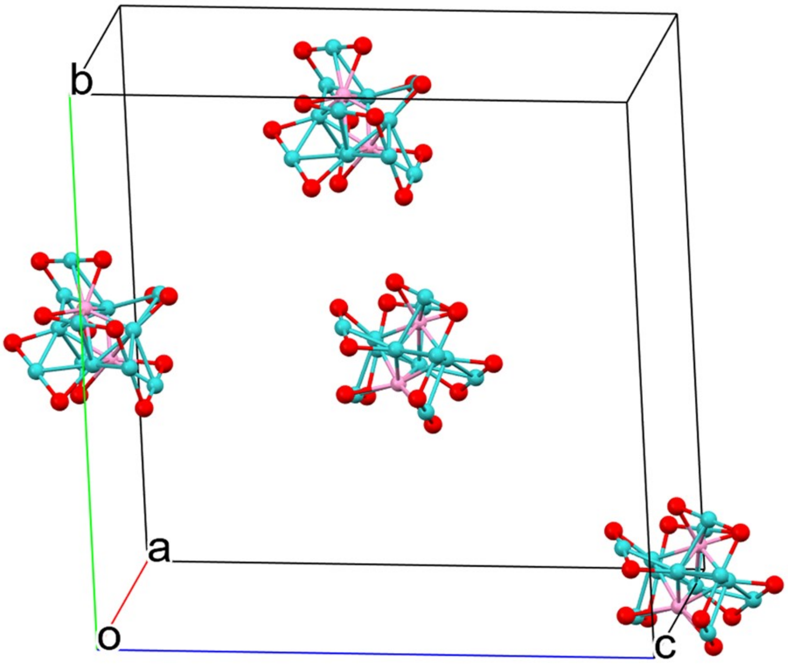

Fig. S21 A unit cell of *R*-$Au_{12}Cd_2$ and label O means the original point of unit cell and labels of a, b, as well as c are the crystal orientation (Color labels: blue = Au, pink = Cd, red = S. All carbon atoms and hydrogen atoms are omitted for clarity).

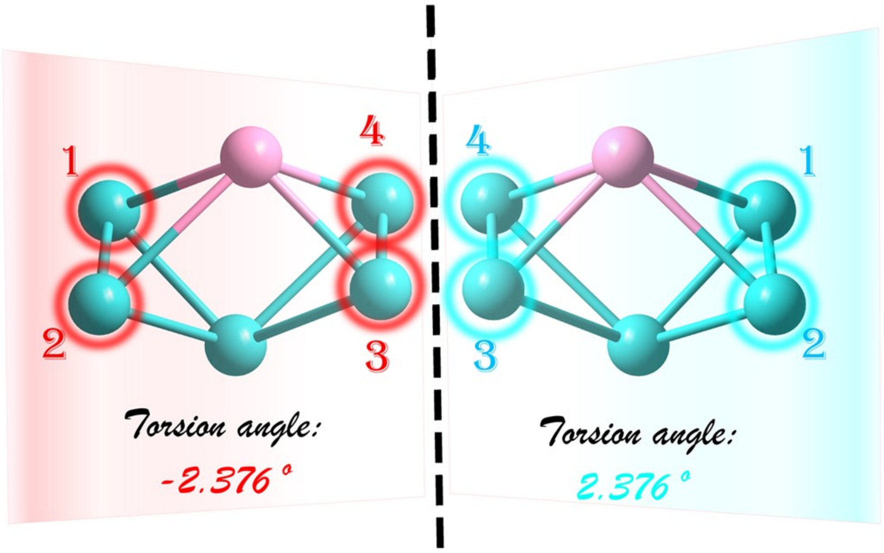

Fig. S22 The torsion angle about core of $Au_{14}Cd_1$, left-hand side is L-configuration and right-hand side is R-configuration (The torsion angle is angle between the plane $Au_1Au_2Au_3$ and $Au_2Au_3Au_4$. Color labels: blue = Au, pink = Cd).

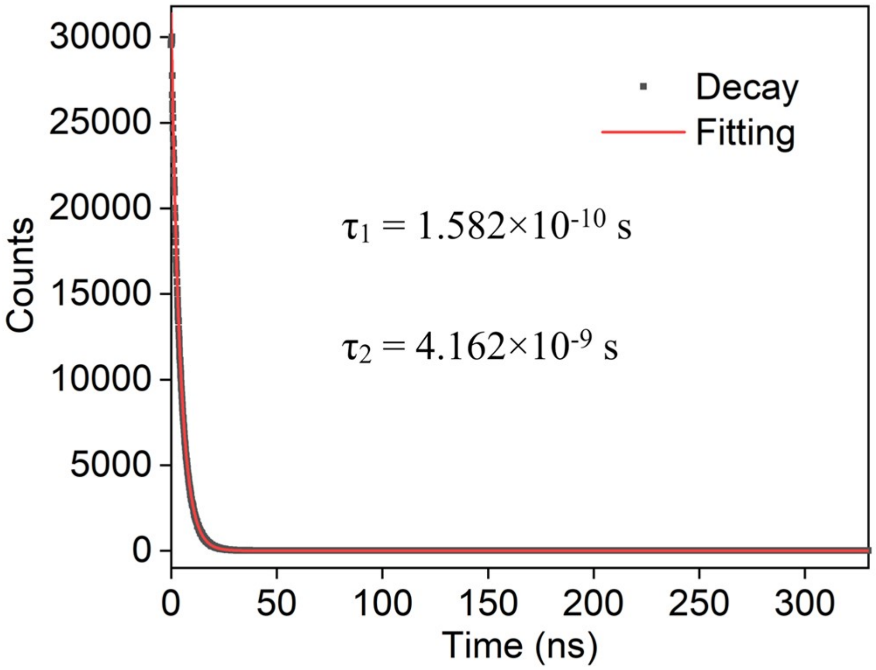

Fig. S23 Fluorescence lifetime of *L*-$Au_{12}Cd_2$ nanocluster.

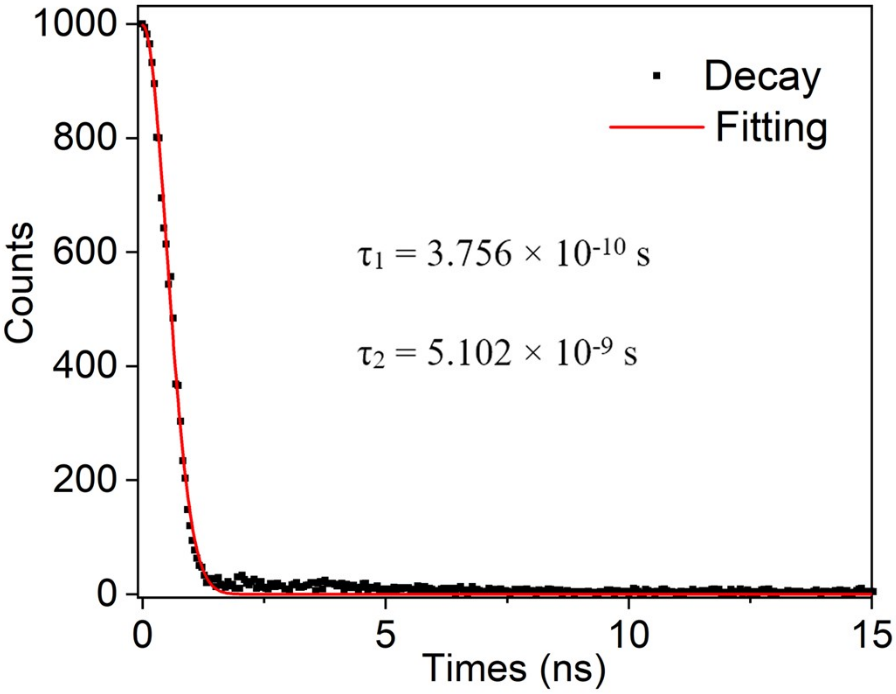

Fig. S24 Fluorescence lifetime of $Au_{14}Cd_1$ nanocluster.

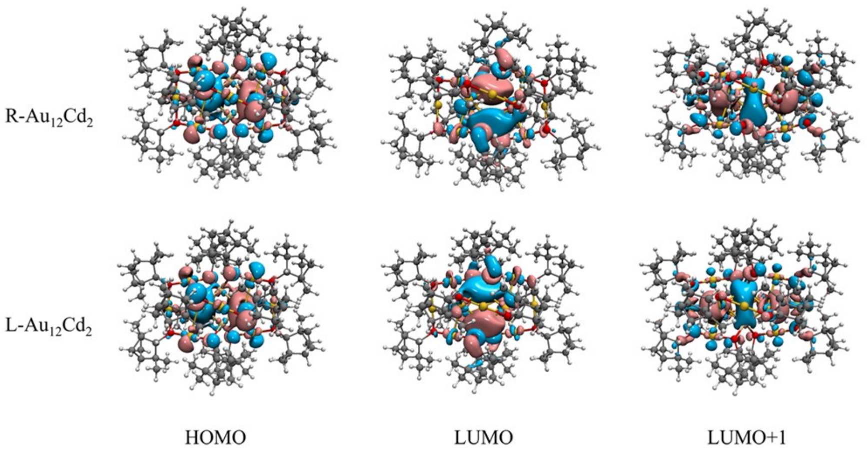

Fig. S25 HOMO to LUMO+1 of *R*-$Au_{12}Cd_2$ and *L*-$Au_{12}Cd_2$ nanoclusters by DFT.

By calculating the fluorescence parameters in R-$Au_{12}Cd_2$ and L-$Au_{12}Cd_2$, it can be found that the oscillator intensity of $S_1 \rightarrow S_0$ is two orders of magnitude smaller than $S_2 \rightarrow S_0$, and the emission energy is also small, which is not conducive to S1 fluorescence radiation, indicating that it may be S_2 fluorescence. From the HOMO-LUMO spectra, it can be seen that HOMO and LUMO+1 orbitals extend in the same direction and overlap to a large extent. Along the extension direction, HOMO has odd symmetry, while LUMO+1 has even symmetry, which makes $S_2 \rightarrow S_0$ have a larger oscillator strength. The extension direction of LUMO is perpendicular to HOMO, with a small degree of overlap, thus the $S_1 \rightarrow S_0$ oscillator strength is small.

The aforementioned front-line orbitals are mainly distributed on the core, and a small amount is distributed on the staple motifs, so whether S_1 or S_2 fluorescence, fluorescence comes from the localized state emission of the core. At present, the intensity of $S_2 \rightarrow S_0$ oscillator is higher, while the intensity and radiation energy of $S_1 \rightarrow S_0$ oscillator are lower, which is more likely to be S_2 fluorescence.

Due to the three mutually perpendicular C_2 axes, R-$Au_{12}Cd_2$ and L-$Au_{12}Cd_2$ can belong to the D_2 point group. Since the oscillator strength f_{em} of $S_1 \rightarrow S_0$ about two nanoclusters is two orders of magnitude smaller than $S_2 \rightarrow S_0$, the emission energy E_{em} is also very small, which is not conducive to S_1 fluorescence radiation according to the energy gap rate, indicating S_2 fluorescence.

Similar results have also been reported in the theoretical work of Pei's group (J. Phys. Chem. Lett. 2022, 13, 16, 3718–3725), considering the fluorescence mechanism of $Au_{28}(CHT)_{20}$. It is worth noting that $Au_{28}(CHT)_{20}$ also has D_2 symmetry. Therefore, the introduction of Cd atoms in the core plays a more significant role in increasing the fluorescence intensity of the nanoclusters. The enhanced fluorescence performance of R/L-$Au_{12}Cd_2$ is caused by the combination of Cd atom doping and chiral ligands modification. However, the main factor that improves the fluorescence properties of R/L-$Au_{12}Cd_2$ is the doping of Cd atoms into the core.

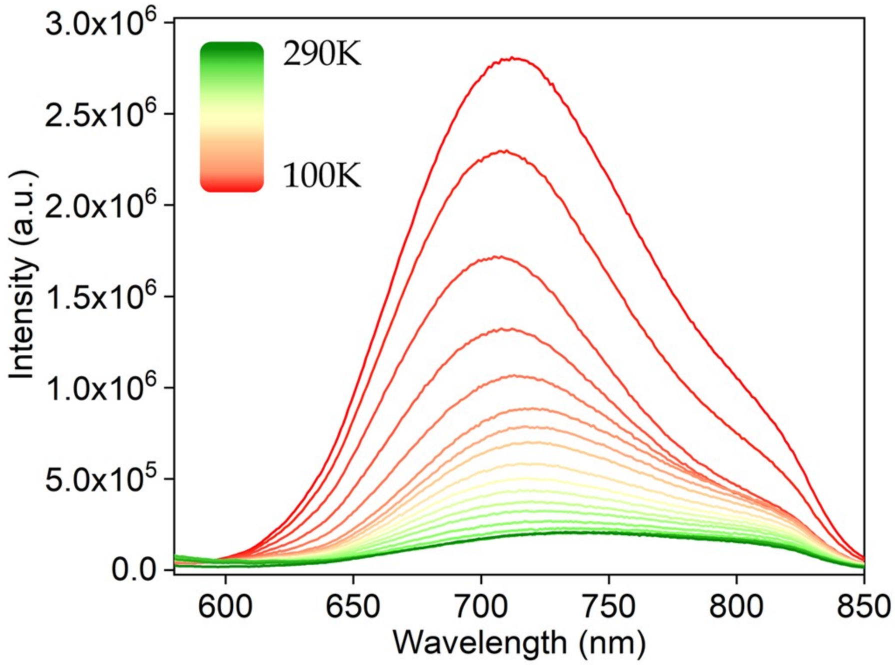

Fig. S26 Temperature-dependent fluorescence spectra of *R*-$Au_{12}Cd_2$ from 100K to 290K.

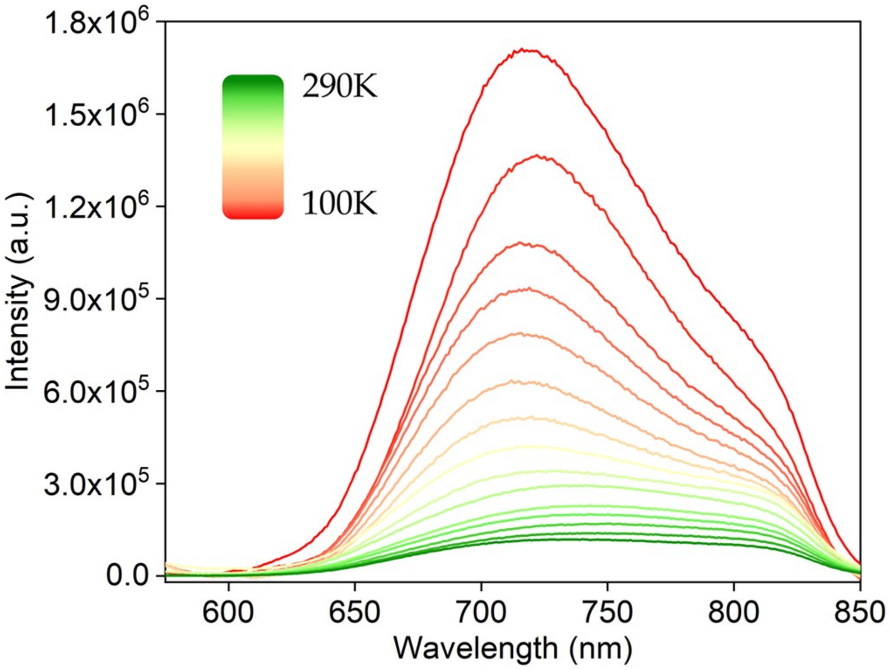

Fig. S27 Temperature-dependent fluorescence spectra of *L*-$Au_{12}Cd_2$ from 100K to 290K.

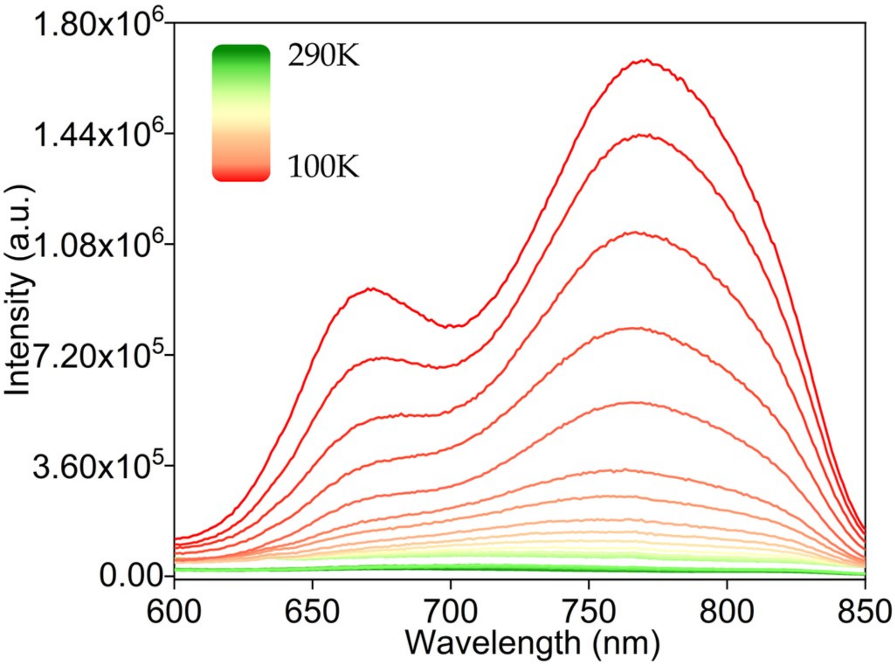

Fig. S28 Temperature-dependent fluorescence spectra of $Au_{14}Cd_1$ from 100K to 290K.

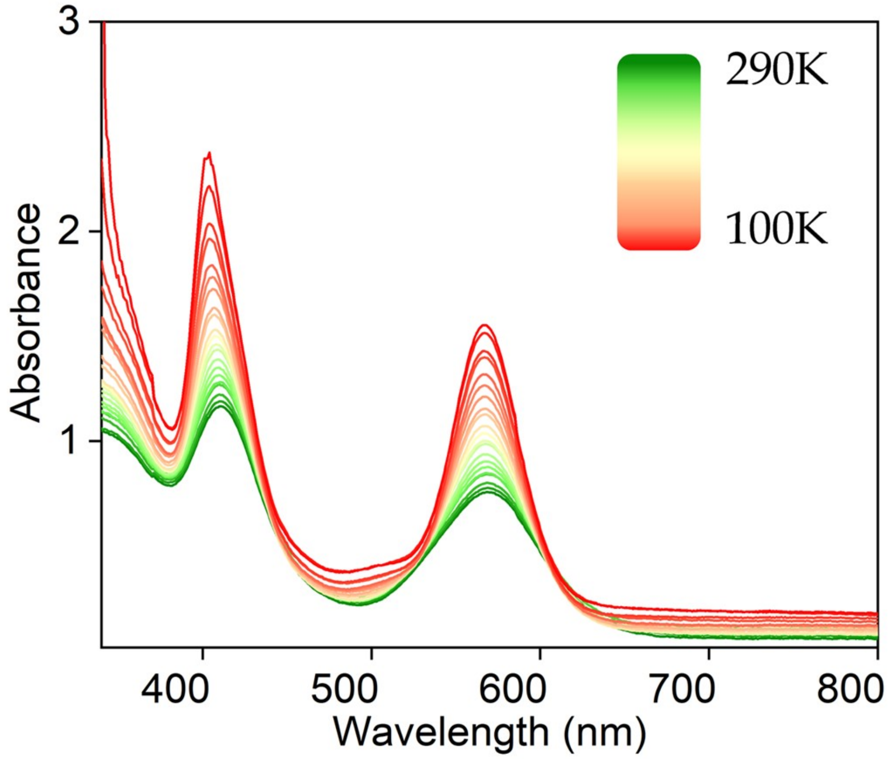

Fig. S29 Temperature-dependent UV-vis absorbance spectra of *R*-$Au_{12}Cd_2$ from 100K to 290K.

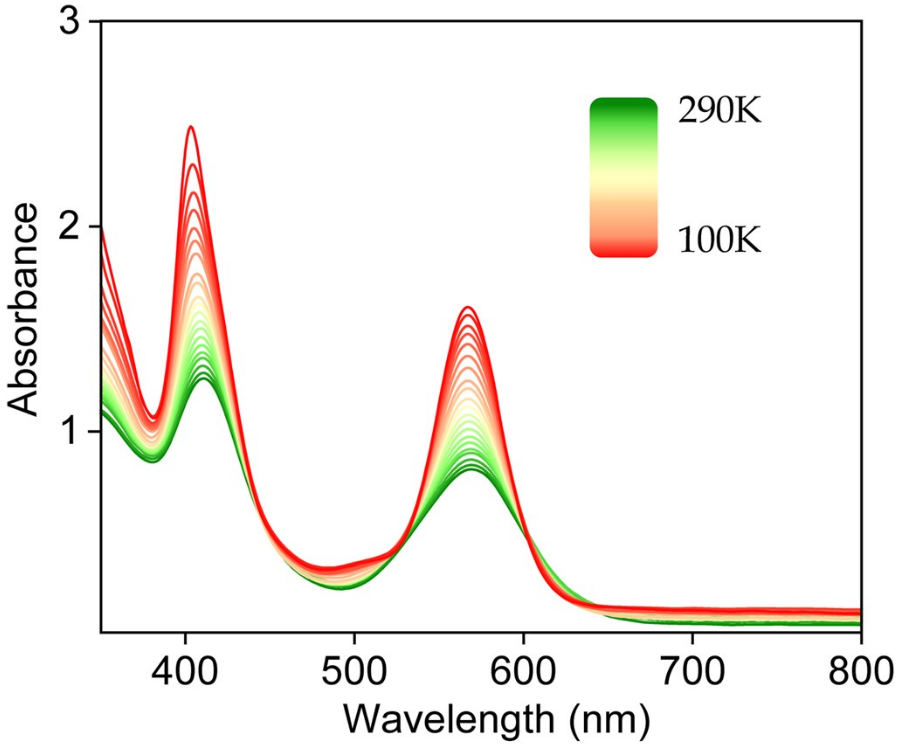

Fig. S30 Temperature-dependent UV-vis absorbance spectra of *L*-$Au_{12}Cd_2$ from 100K to 290K.

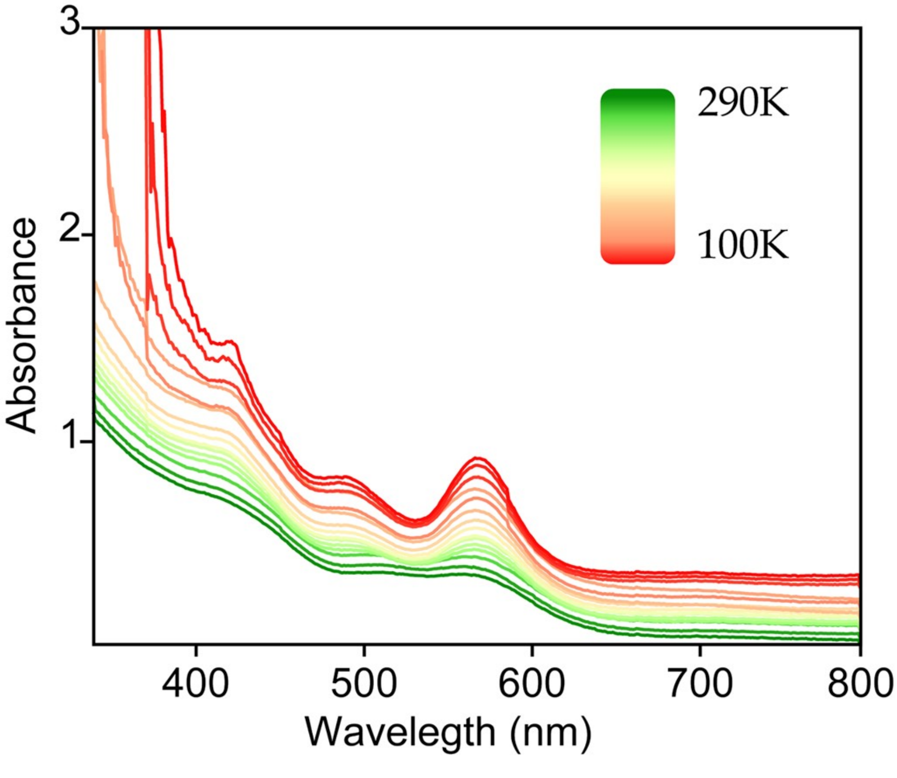

Fig. S31 Temperature-dependent UV-vis absorbance spectra of $Au_{14}Cd_1$ from 100K to 290K.

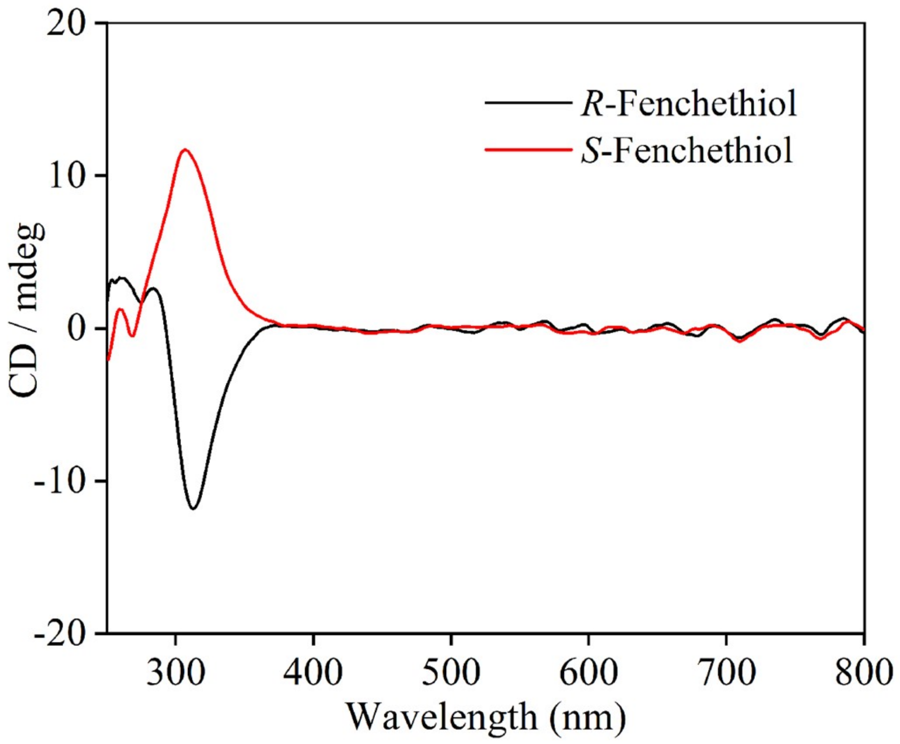

Fig. S32 Circular dichroism spectra of Fenchethiol ligands (red line is *S*-configuration and black line is *R*-configuration).

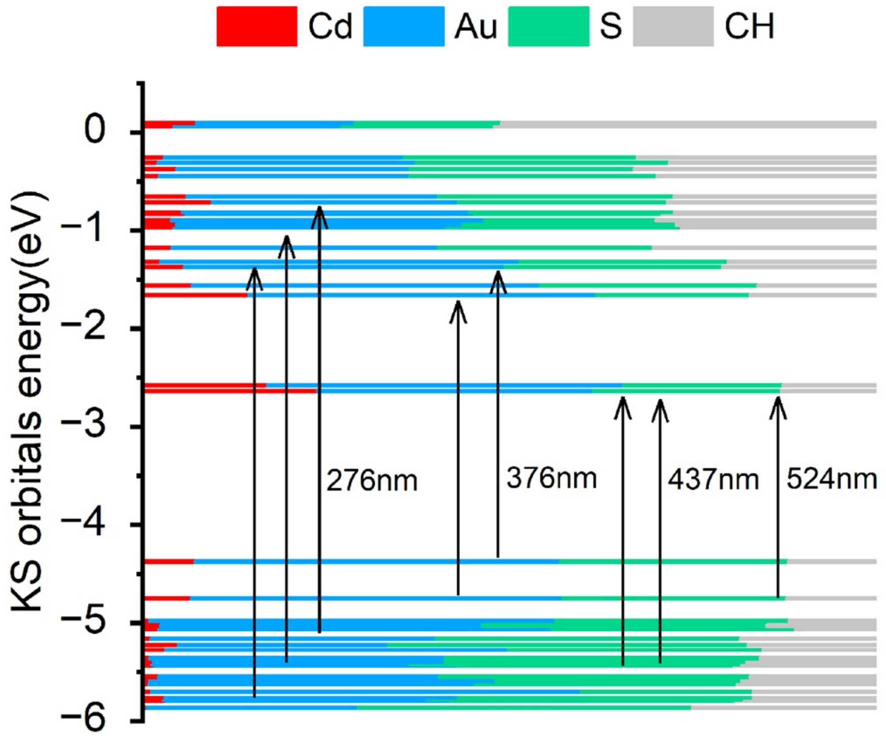

Fig. S33 Kohn-Sham molecular orbital energy level diagram of *L*/*R*-$Au_{12}Cd_2$ for circular dichroism.

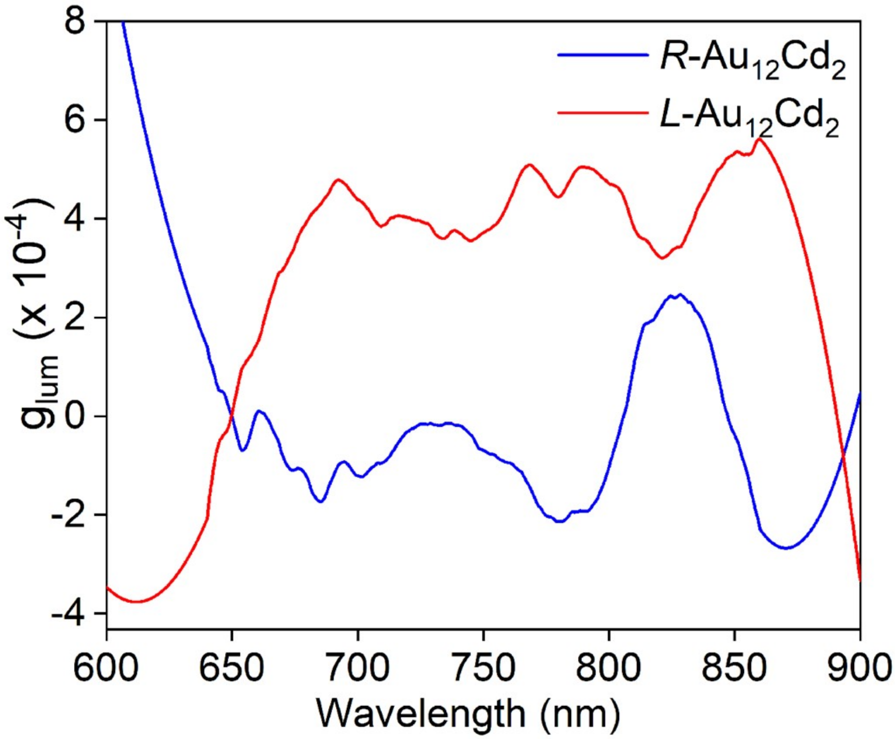

Fig. S34 The g_{lum} of *L*-$Au_{12}Cd_2$ (red trace) and *R*-$Au_{12}Cd_2$ (blue trace).

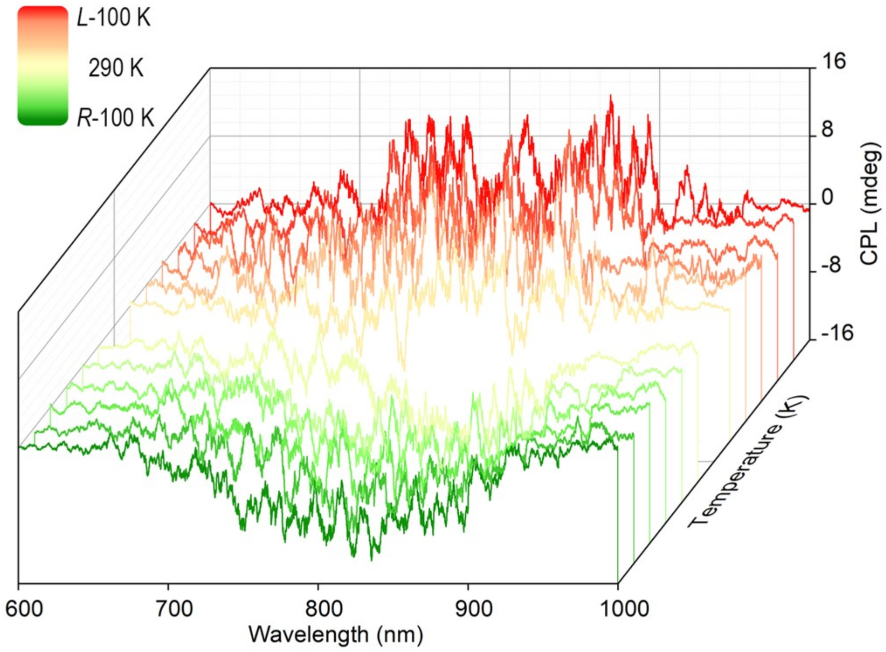

Fig. S35 Temperature-dependent circularly polarized luminescence spectra of *R/L*-$Au_{12}Cd_2$ from 290 to 100 K.

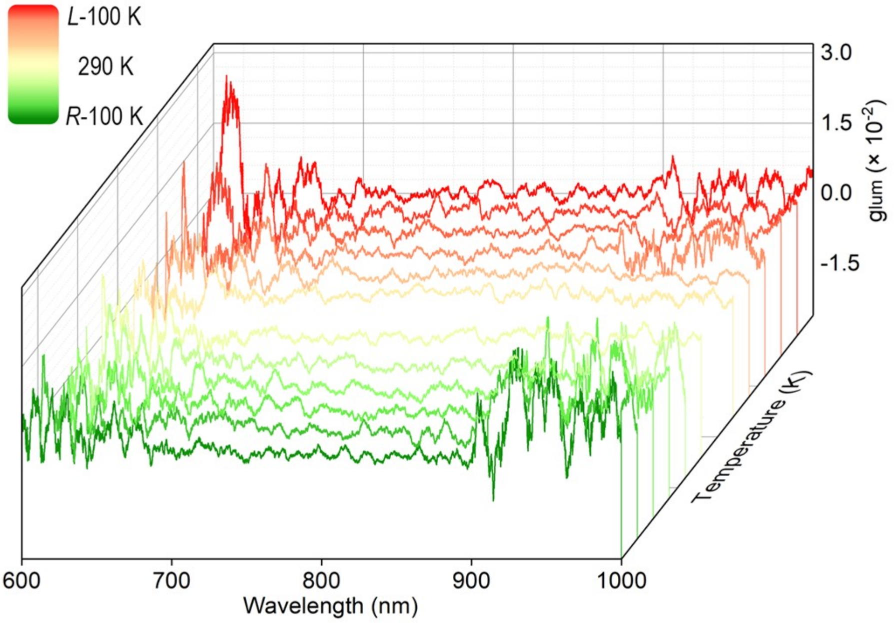

Fig. S36 Temperature-dependent g_{lum} of *R*/*L*-$Au_{12}Cd_2$ from 290 to 100 K.

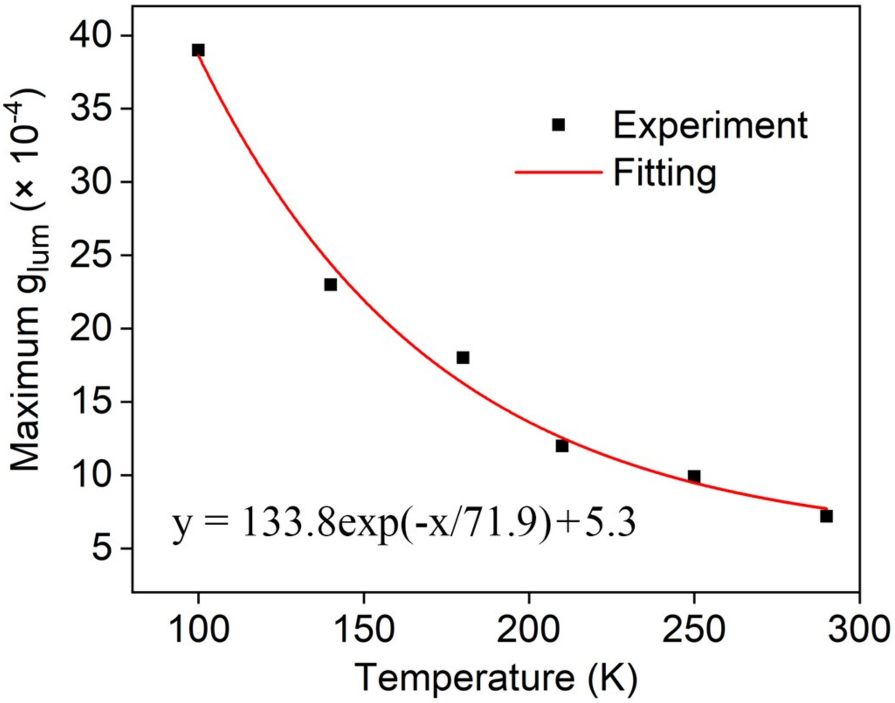

Fig. S37 Temperature-dependent maximum g_{lum} of *R*/*L*-$Au_{12}Cd_2$ at from 290 to 100 K, and the derived formulas for the temperature (x) and maximum g_{lum} (y) changes.

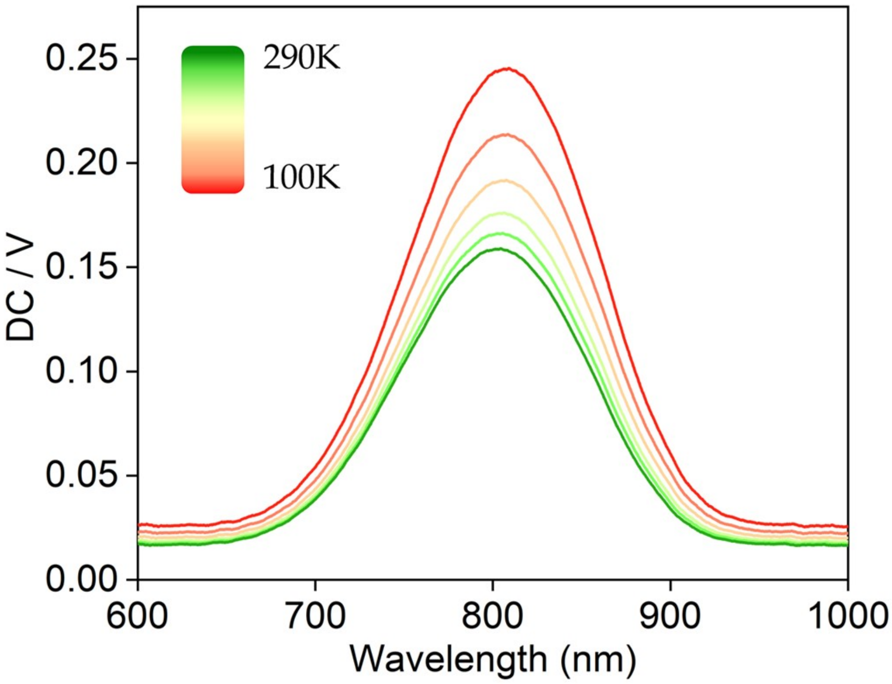

Fig. S38 Temperature-dependent DC spectra of $Au_{12}Cd_2$ at from 290 to 100 K.

Table S1 The values of observer strength and major orbital contributions of *L/R*-$Au_{12}Cd_2$ for absorption at different wavelength were calculated by DFT.

Wavelength (nm)	Oscillator Strength (in cgs)	Major orbital contributions
374 nm	0.0744	HOMO-1→LUMO+3(54%), HOMO→LUMO+5(10.3%)
639 nm	0.0904	HOMO→LUMO+1(90.9%)

Table S2 Crystal data and structure refinement for $Au_{12}Cd_2(S\text{-}C_{10}H_{17}S)_{12}$ nanocluster.

CCDC	2266860
Empirical formula	$C_{120}H_{204}Au_{12}Cd_2S_{12}$
Formula weight	4619.94
Temperature/K	293(2)
Crystal system	orthorhombic
Space group	$P2_12_12_1$
a/Å	22.8453(3)
b/Å	23.7930(3)
c/Å	26.4043(3)
α/°	90
β/°	90
γ/°	90
Volume/$Å^3$	14352.3(3)
Z	4
$\rho_{calc}g/cm^3$	2.138
μ/mm^{-1}	26.654
F(000)	8640.0
Crystal size/mm^3	0.08 × 0.07 × 0.01
Radiation	CuKα (λ = 1.54186)
2Θ range for data collection/°	7.658 to 136.332
Index ranges	$-22 \le h \le 27, -21 \le k \le 28, -31 \le l \le 23$
Reflections collected	115272
Independent reflections	25544 [R_{int} = 0.0612, R_{sigma} = 0.0713]
Data/restraints/parameters	25544/1683/1337
Goodness-of-fit on F^2	0.972
Final R indexes [I>=2σ (I)]	R_1 = 0.0655, wR_2 = 0.1687
Final R indexes [all data]	R_1 = 0.0846, wR_2 = 0.1765
Largest diff. peak/hole / e $Å^{-3}$	2.21/-1.73
Flack parameter	-0.007(17)

Table S3 Crystal data and structure refinement for $Au_{12}Cd_2(R\text{-}C_{10}H_{17}S)_{12}$ nanocluster.

CCDC	2266865
Empirical formula	$C_{120}H_{204}Au_{12}Cd_2S_{12}$
Formula weight	4619.94
Temperature/K	120
Crystal system	monoclinic
Space group	$P2_1$
a/Å	19.1684(3)
b/Å	27.7216(3)
c/Å	28.1292(4)
α/°	90
β/°	98.3240(10)
γ/°	90
Volume/Å^3	14789.8(4)
Z	4
ρ_{calc}g/cm^3	2.075
μ/mm^{-1}	25.865
F(000)	8640.0
Crystal size/mm^3	0.1 × 0.09 × 0.01
Radiation	CuKα (λ = 1.54186)
2Θ range for data collection/°	7.9 to 139.196
Index ranges	$-23 \leq h \leq 16$, $-24 \leq k \leq 33$, $-31 \leq l \leq 34$
Reflections collected	121072
Independent reflections	46417 [R_{int} = 0.0687, R_{sigma} = 0.0959]
Data/restraints/parameters	46417/1976/2684
Goodness-of-fit on F^2	1.048
Final R indexes [I>=2σ (I)]	R_1 = 0.0810, wR_2 = 0.1993
Final R indexes [all data]	R_1 = 0.0988, wR_2 = 0.2288
Largest diff. peak/hole / e Å^{-3}	3.48/-3.82
Flack parameter	-0.03(2)

Table S4 The fluorescence parameters of *R*-$Au_{12}Cd_2$ and *L*-$Au_{12}Cd_2$ were summarized by DFT.

	E_{em} ($S_1\rightarrow S_0$)	λ_{em} ($S_1\rightarrow S_0$)	f_{em} ($S_1\rightarrow S_0$)	E_{em} ($S_2\rightarrow S_0$)	λ_{em} ($S_2\rightarrow S_0$)	F_{em} ($S_2\rightarrow S_0$)
L-$Au_{12}Cd_2$	0.542 eV	2285.6 nm	0.0005	1.312 eV	945 nm	0.031
R-$Au_{12}Cd_2$	0.610 eV	2032.7 nm	0.0007	1.301 eV	953 nm	0.024

Table S5 The fluorescence parameters about $S_1 \rightarrow S_0$ of *R*-$Au_{12}Cd_2$ and *L*-$Au_{12}Cd_2$ were summarized by DFT.

$S_1 \rightarrow S_0$	Wavelength	Oscillator Strength	Major orbital contributions
L-$Au_{12}Cd_2$	2286 nm	0.0005	LUMO→HOMO (99.9%)
R-$Au_{12}Cd_2$	2032 nm	0.0007	LUMO→HOMO (99.8%)

Table S6 The fluorescence parameters about $S_2 \rightarrow S_0$ of *R*-$Au_{12}Cd_2$ and *L*-$Au_{12}Cd_2$ were summarized by DFT.

$S_2 \rightarrow S_0$	Wavelength	Oscillator Strength	Major orbital contributions
L-$Au_{12}Cd_2$	945 nm	0.031	LUMO+1→HOMO (65.83%)
R-$Au_{12}Cd_2$	953 nm	0.024	LUMO+1→HOMO (70.20%)

Table S7 The values of observer strength and major orbital contributions at different wavelength of *L/R*-$Au_{12}Cd_2$ for circular dichroism were calculated by DFT.

	Wavelength (nm)	Rotatory Strength (in cgs)	Major orbital contributions
a	276 nm	73.48	HOMO-18→LUMO+5(16.35%), HOMO-10→LUMO+8(16.31%), HOMO-5→LUMO+13(11.45%)
b	376 nm	76.45	HOMO-1→LUMO+3(50.04%), HOMO→LUMO+5(10.30%)
c	437 nm	44.41	HOMO-11→LUMO (77.14%), HOMO-10→LUMO (11.57%)
d	524 nm	-7.05	HOMO-2→LUMO (90.16%)

Table S8 Summarizes of the maximum anisotropy factors of partial reported chiral nanoclusters.

NCs	$Au_{12}Cd_2$ (This work)	$Ag_{24}Au_1$ (2)	$AuCu_4$ (3)	Ag_{17} (4)	Pt_2Ag_3 (5)	Au_{13} (6)
Maximum anisotropy factors	5.8×10^{-4}	1.5×10^{-4}	9.0×10^{-4}	1.2×10^{-3}	1.8×10^{-3}	3×10^{-3}

References

1 J. Li, P. Wang, Y. Pei, *J. Phys. Chem. Lett.*, 2022, **13**, 3718–3725.

2 K. R. Krishnadas, L. Sementa, M. Medves, A. Fortunelli, M. Stener, A. Fürstenberg, G. Longhi and T. Bürgi, *ACS Nano,* 2020, **14**, 9687–9700.

3 X.-H. Ma, J. Li, P. Luo, J.-H. Hu, Z. Han, X.-Y. Dong, G. Xie and S.-Q. Zang, *Nat. Commun.,* 2023, **14**, 4121.

4 M.-M. Zhang, X.-Y. Dong, Z.-Y. Wang, X.-M. Luo, J.-H. Huang, S.-Q. Zang and T. C. W. Mak, *J. Am. Chem. Soc.,* 2021, **143**, 6048–6053.

5 S. Horiuchi, S. Moon, A. Ito, J. Tessarolo, E. Sakuda, Y. Arikawa, G. H. Clever and K. Umakoshi, *Angew. Chem. Int. Ed.,* 2021, **60**, 10654–10660.

6 S. Li, X.-Y. Dong, K.-S. Qi, S.-Q. Zang and T. C. W. Mak, *J. Am. Chem. Soc.,* 2021, **143**, 20574–20578.